

This article appeared in a journal published by Elsevier. The attached copy is furnished to the author for internal non-commercial research and education use, including for instruction at the authors institution and sharing with colleagues.

Other uses, including reproduction and distribution, or selling or licensing copies, or posting to personal, institutional or third party websites are prohibited.

In most cases authors are permitted to post their version of the article (e.g. in Word or Tex form) to their personal website or institutional repository. Authors requiring further information regarding Elsevier's archiving and manuscript policies are encouraged to visit:

<http://www.elsevier.com/copyright>



ELSEVIER

Available online at www.sciencedirect.com
**PHOTONICS AND
NANOSTRUCTURES**
Fundamentals and Applications

Photonics and Nanostructures – Fundamentals and Applications 6 (2008) 19–25

www.elsevier.com/locate/photronics

Photonic crystal waveguides for coarse-selectivity devices

M. Ayre^a, C. Cambournac^a, O. Khayam^a, H. Benisty^{a,*}, T. Stomeo^b, T.F. Krauss^b
^a*Laboratoire Charles Fabry de l'Institut d'Optique, CNRS, Univ Paris-Sud, Campus Polytechnique, RD 128, F-91127 Palaiseau, France*
^b*School of Physics & Astronomy, University of St. Andrews, St. Andrews KY16 9SS, UK*

Received 15 June 2007; received in revised form 4 September 2007; accepted 11 September 2007

Available online 16 September 2007

Abstract

We discuss devices based on photonic crystal planar waveguides for use as wavelength-selective applications via the mini-stopband extraction mechanism. We present experimental data for the core of a compact demux system. We show that spatial and spectral behaviours are as intended from coupled-mode theory, as well as from the finite-difference time-domain approach. Finally, we propose architectures with large crosstalk and some inherent fabrication-related advantages achieved by duplicating the basic multimode waveguide and using it as a spectral filter.

© 2007 Elsevier B.V. All rights reserved.

PACS : 84.40.Ua; 42.79.Sz; 42.82.Et; 42.79.Gn

Keywords: Photonic crystals; Demultiplexing; Multimode waveguide

1. Introduction

Indium phosphide (InP) and related III–V compounds have interesting features for the practical implementation of photonic devices with various active functions such as photodetection, tunability, nonlinearity, and carrier injection for gain and lasing. As such integration is very relevant to frequency-selective devices, we use this, rather than silicon, as the platform for our investigation.

Here we discuss experimental data for the core of a compact demux system, with only modest resolution (a few nanometers), based on the mini-stopband (MSB) effect taking place in a multimode photonic crystal (PhC) planar waveguide. Our previous papers [1–3] were focussed on results obtained from the internal light source (ILS) technique, with some intrinsic losses due to the embedded luminescent layers.

We now make use of a standard end-fire technique on a passive system, using standard tapering and bending techniques to integrate our devices into an optical circuit. We observe spatial and spectral behaviours that are in good agreement with coupled-mode theory (CMT). Additionally, the integration of the device, together with finite-difference time-domain (FDTD) simulations, allows us to gain physical insight into effects that were previously damped in the ILS technique. Notably, the contrasted differential behaviour of MSB centre and MSB edges is well rendered. Furthermore, using coupled-mode analysis, we show that the crosstalk is intrinsically limited by the “singly resonant” behaviour of the device. We thus propose a “doubly resonant” architecture which enables large crosstalk and possesses some inherent fabrication-related advantages. It is based on duplicating the basic multimode waveguide on the exit path of the extracted light, for use as a spectral filter. Crosstalk performances better than 30 dB are expected between coarse WDM channels.

* Corresponding author.

E-mail address: henri.benisty@institutoptique.fr (H. Benisty).

2. Singly resonant mini-stopband-based demultiplexing device

2.1. Reminder of device operation, previous works, and HOM maps

The mini-stopband (MSB) effect originates from energy transfer between the fundamental mode and a higher order mode of a multimode PhC waveguide, as illustrated in Fig. 1. We recall in Fig. 1a a generic photonic crystal waveguide band structure (e.g. three-missing rows along ΓM , also named “W3” below), where the trajectory of the fundamental mode dispersion and its folding at zone edge are sketched as well. The higher order mode dispersion starts like a Fabry–Perot mode would. Then it anticrosses with the fundamental mode and defines the MSB. The coupling and subsequent energy transfer require frequency and k -matching of the dispersion relation of both modes, hence taking place for a single frequency and parallel wavevector combination (Fig. 1a). More exactly, this diffraction phenomenon takes place at the anticrossing of both dispersion bands, creating a localized photonic bandgap, as explained in previous work [4].

Then, as pictured in Fig. 1b, such a coupling effect can be used for demultiplexing (demux) by thinning the PhC wall on one side of the waveguide to achieve adequate leakage of the higher order mode.

This technique exhibits several advantages with respect to conventional demux devices [5,6], at least for coarse filtering or single-frequency extraction/monitoring. Essentially, even compact arrayed waveguide gratings (AWG) must significantly increase their footprint to achieve good crosstalk performance. Equally, we can compare this methodology to other PhC demultiplexers, either waveguide- [7,8] or superprism-based [9,10]. As we work with large-area waveguides, our approach is more robust to fabrication-limited coupling problems than the former, and provides more natural integration possibilities than the latter.

To efficiently model the device, with respect to the effects of MSB width, coupling coefficients, and losses, we use a coupled-mode formalism, as elaborated in Ref. [11] from Ref. [12]. The evolution of the higher order mode (HOM), denoted $S(z)$, and of the fundamental mode, $R(z)$, are then described by the following coupled-mode equations:

$$\begin{aligned} \frac{dR}{dz} &= \left[-i(k_0 - k_r) - \frac{\alpha_r}{2} \right] R - i\kappa S \\ \frac{dS}{dz} &= \left[-i(k_0 - k_s) + \frac{\alpha_s}{2} \right] S + i\kappa R \end{aligned} \quad (1)$$

where the propagation constants of the uncoupled modes are $k_r(u)$ and $k_s(u)$ (where the frequency dependence is related to group indices n_r and n_s , respectively), ω_0 is the Bragg frequency (the intersection point of Fig. 1a) and κ is the coupling constant. The respective loss coefficients are α_r and α_s .

In this paper, we use CMT and check it experimentally and against FDTD simulation of a device with realistic terminations of the useful waveguide section. As a reminder, Fig. 2 shows typical HOM and fundamental mode maps obtained from CMT. It clearly highlights the expected MSB effect caused by the multimode PhC waveguide: as the input signal frequency approaches the MSB centre, energy is coupled to the HOM with maximal efficiency at the Bragg frequency $u_0 = a/\lambda = 0.27$. Conversely, at the MSB edges the coupling constant is significantly lower and hence the characteristic extraction length increases.

A multi-channel demux can be simply obtained by cascading sections, such as that in Fig. 1b, with a small change in width (Fig. 1c). Such a change only inflicts a minor penalty to the energy flow of the fundamental mode, while it shifts the higher order mode dispersion band and thus the MSB characteristic frequency upwards. Because there is still a sizable – albeit slow – negative group velocity of the counter-propagating HOM, due to the MSB finite $k_{||}$ -value, the HOM is generated from the end of each section (Fig. 1c) from the interaction of the fundamental mode and the resonantly tuned PhC waveguide. It grows backward to a maximal value as in classical contra-directional coupling. On the upstream side (towards the bottom of Fig. 1c), the HOM still propagates slowly but no further generation occurs as the off-resonance PhC waveguide situation for the fundamental mode pump frequency. The HOM then decays in the upstream section at a spatial rate that depends on losses, which in turn depend inversely on the group index n_s of the HOM.

The issue of a good multi-section design has recently been partly addressed elsewhere [3,13], but the crosstalk is obviously another issue to consider. In other words, understanding the details of generation and propagation of an HOM at some nominal frequency in an adjacent channel, *i.e.*, at the “bad” frequency, is obviously of interest to reach good performances *a priori*, namely by a proper design. To this end, two kinds of design can be sought: either full demux, where everything is dropped in the designed section, or monitoring, where the fundamental mode is transmitted with ~ 1 dB attenuation and a weaker

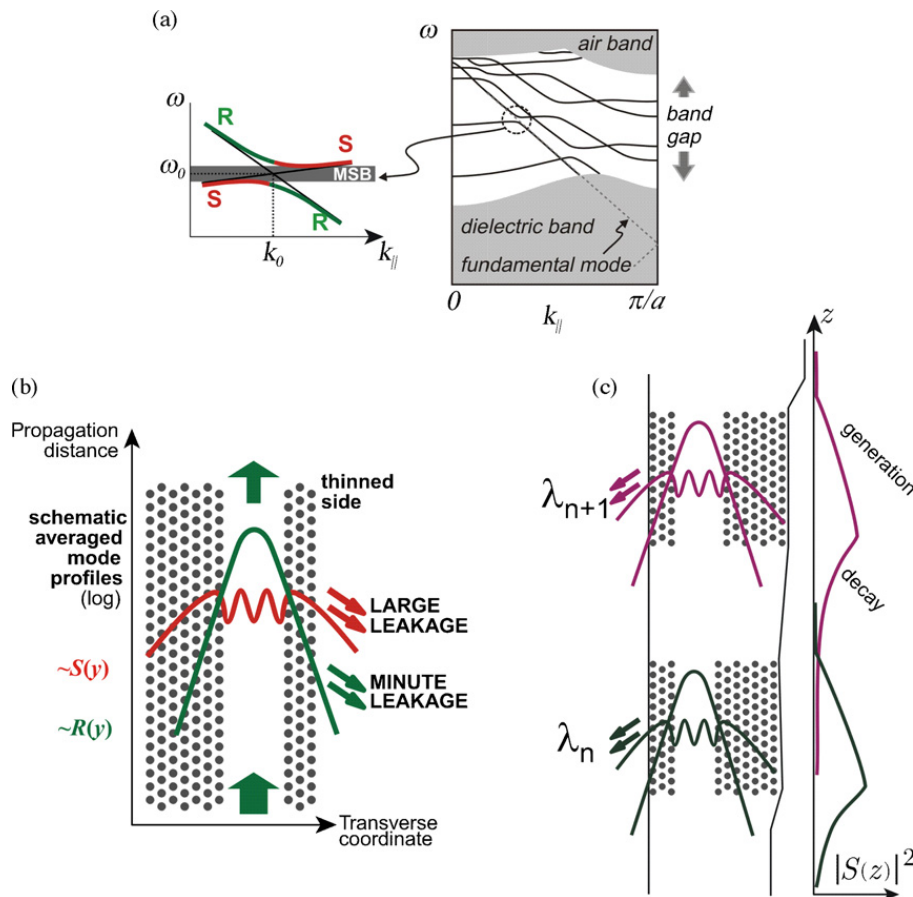


Fig. 1. Principle of MSB effect and its application to demux operation. (a) Overall band structure of a typical photonic crystal waveguide (e.g. W3) along the ΓM direction, the fundamental mode is indicated as a grey dashed line, folded at the zone edge, with a zoom on the MSB anticrossing. (b) At the specific MSB frequency only, the higher order mode S is generated by coupling to the fundamental mode R, and is extracted across the thinned side of the device. (c) Multi-section case (two sections illustrated). The backwards generation of the higher order mode occurs due to the fundamental mode–PhC interaction, its decay (still backwards) occurs everywhere and is the sole mechanism as the changed PhC waveguide section now inhibits further generation.

extracted signal (~ -10 dB) is generated for monitoring.

We suggested in Ref. [3] that the extraction itself has to be taken into account, amongst the loss factors, as it

leads to a damping of the HOM. We shall further discuss this point but it should be noted that in the CMT equations we use an overall attenuation coefficient $\alpha_s = \alpha_s^i + \alpha_s^e$ that captures both intrinsic (α_s^i) and extraction (α_s^e) losses.

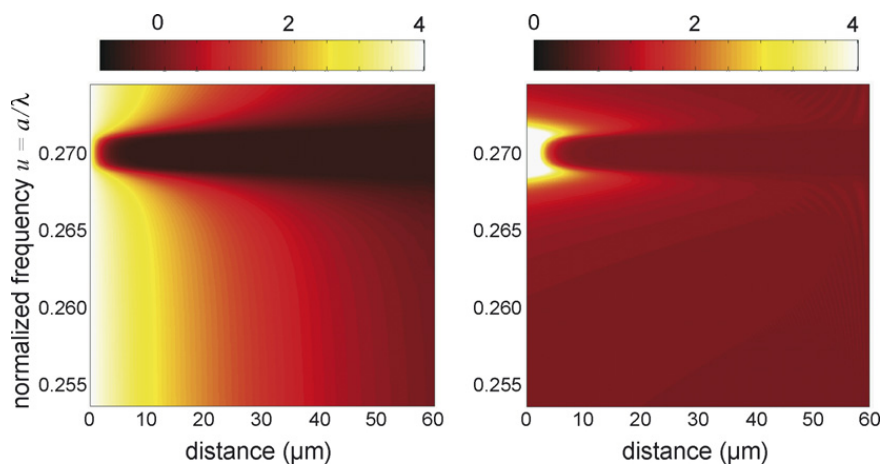


Fig. 2. Evolution maps showing the MSB effect as a function of the propagation length and normalized optical frequency. Left: Fundamental mode. Right: Higher order mode. The MSB is centred here on a Bragg frequency $u_0 = 0.27$.

2.2. End-fire measurements

Experimentally, we used an InP-based heterostructure, consisting of a monomode GaInAsP guiding layer on an InP substrate and capped by a 300 nm-thick InP top cladding. The effective phase index of the fundamental transverse mode of the heterostructure is $n = 3.21$ at $\lambda = 1550$ nm. We consider a photonic crystal waveguide defined by removing three rows of holes along the ΓK direction, with the cladding on one side thinned to only three rows of holes to permit the extraction of the HOM. The holes defining a “W3” three-missing-rows waveguide were written using a Raith Elphy e-beam tool in ZEP520 positive resist and transferred into a spin-on-glass hardmask using reactive-ion etching (RIE) in fluorine chemistry, before being deep-etched by Ar + Cl₂ in chemically assisted ion-beam etching (CAIBE), as described earlier in Ref. [14]. An air fill factor of 36% was achieved. The sample layout and device design are shown in Fig. 3. Note that the device is tilted by means of the bends seen in the micrograph such that the extraction angle of the centre frequency is normal to the cleaved facet.

Fig. 4 illustrates the implemented set-up for the end-fire characterization of our samples. Light is delivered by an external-cavity laser source (ECL, Ando AQ-8201-13), continuously tuneable from 1460 to 1580 nm,

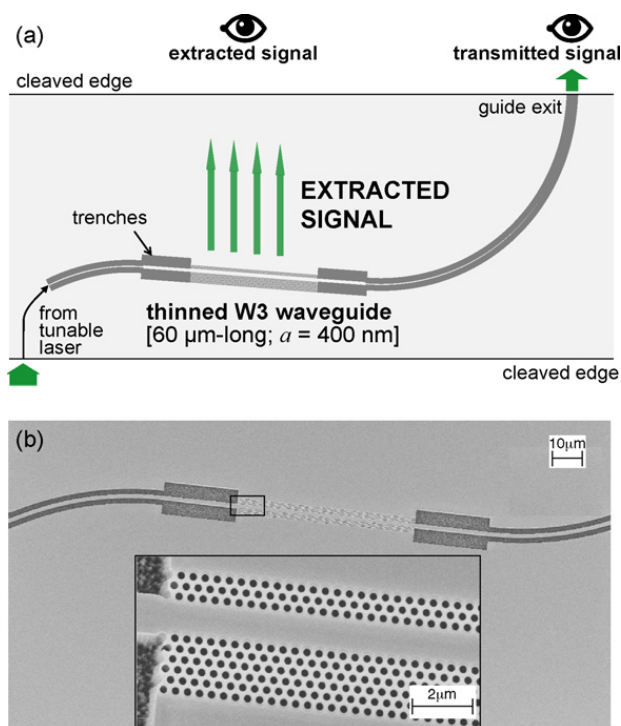


Fig. 3. Device design and sample layout. (a) Illustration of device design (top view). (b) Sample layout (inset shows a zoomed micrograph of the input of the fabricated PhC waveguide).

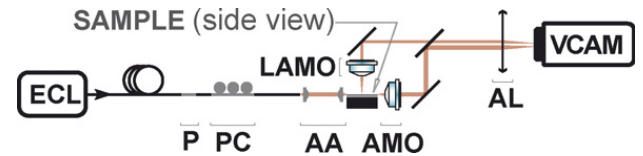


Fig. 4. Illustration of the experimental set-up (side view). Elements: ECL, tunable laser source; P, polarizer; PC, polarization controller; AA, piezoelectrically controlled aspheric achromatic telescope for focusing and injection; AMO, achromatic microscope objective [$\times 20$ –0.35 NA] for output collection and re-injection for spectral analysis; LAMO, long working distance achromatic microscope objective [$\times 20$ –0.40 NA] for top imaging; AL, achromatic imaging lens; VCAM, Vidicon fluorescent camera.

and a combination of an aspheric NIR achromatic moulded lens (NA = 0.55) and a NIR achromatic microscope objective (NA = 0.35) to couple light into and out of the circuit. At the output, either the side-extracted or the transmitted signal can be collected at will by simple translation along the cleaved facet. The pattern seen on the side using a Vidicon camera (Hamamatsu C-2400-03) exhibited dramatic variations as a function of wavelength. Typical extraction patterns are shown in Fig. 5. We filtered this part of the image and carefully subtracted background. It was then averaged over ~ 10 pixels vertically to get a map representing the local HOM value $|S(z)|^2$ as a function of frequency (see Fig. 5c). We see extracted light at the

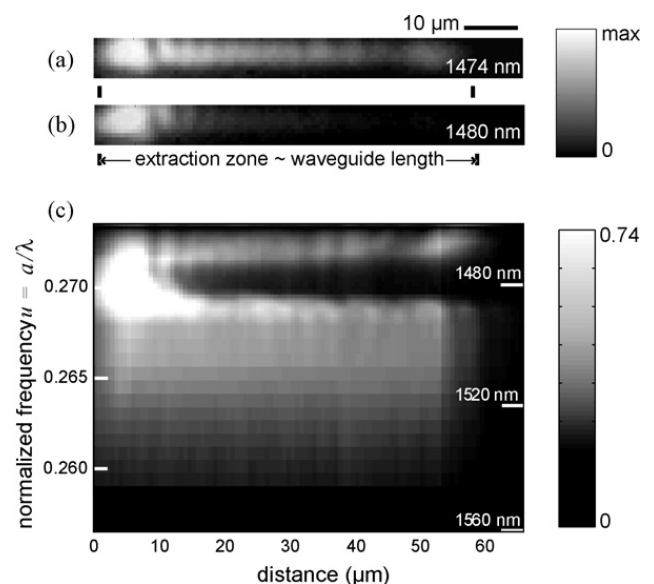


Fig. 5. Typical extraction patterns imaged at the output facet of the device for two wavelengths. (a) 1474 nm: beginning of extraction at MSB upper edge leading to variation (generation/decay) at a large scale compared to waveguide length L . (b) 1480 nm: best extraction efficiency at Bragg frequency for which characteristic length is minimal and lower than L . (c) Extraction map as a function of normalized frequency.

input side of the device, across the whole MSB frequency region, whereas we see a signal extended across the device length only for frequencies at the edges of the MSB. This is the first such experiment on a fully passive externally injected system, unlike the prior results of Ref. [3].

2.3. Analysis of image in relation with HOM map

To understand the details of the experimental response, we consider a 2D FDTD calculation using CrystalWave software [15]. The dielectric profile matches the experimental device layout, and we use an effective index of the fundamental transverse mode of 3.21. At some distance above the thinned side of the waveguide, we record the response to an input pulse as a function of time for a line of grid points parallel to the waveguide propagation axis. By performing a Fourier transform for each of these points, we can build up a map of the intensity versus frequency and position, which relates qualitatively to the experiment and proportionally to the HOM intensity $|S(z)|^2$.

Fig. 6 shows the result of such calculation to be compared with the experimental one (Fig. 5c). We note that the MSB centre position is slightly shifted with respect to the experiment, which we attribute to the usual error in measuring the fill factor, rather than dispersion effects neglected in this 2D model. As discussed above for CMT and experiment, we again see the characteristic shape of the CMT HOM map, showing the rapid depletion of the fundamental mode at the MSB centre and the long tails of the extraction at the edges of the MSB.

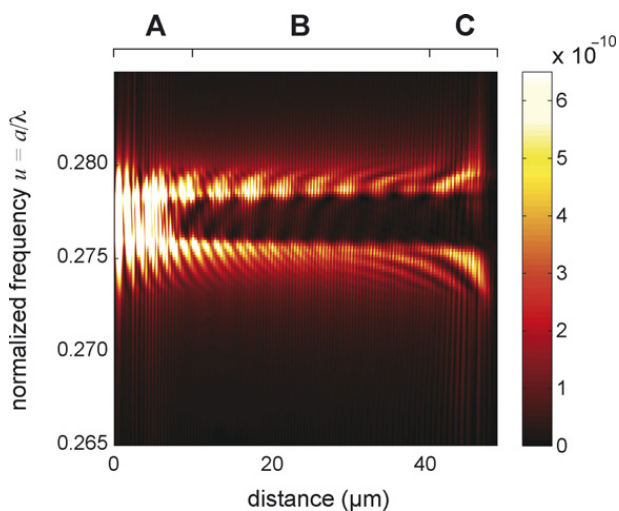


Fig. 6. Extraction map of the HOM obtained by FDTD simulation. Again, we see the characteristic shape of the MSB depletion, but additionally we see nodes in the response which are asymmetric with respect to the centre frequency.

However, the intensity profile is not symmetric with respect to the Bragg frequency, in agreement with the experiment (zone B) but contrary to the CMT. Furthermore, we see zeros in intensity near the input side (zone A), and a slight increase of the intensity towards the output side (zone C). By observing the propagation of the steady-state field at various frequencies, we find that the zeros in zone A are caused by interference originating from the reflection of the backward-propagating extracted signal from the trenches defining the ridge waveguide at the input of the device (see Fig. 3). Note that this is a different effect to the impedance mismatch in-coupling reflection observed experimentally in Ref. [16]. In zone C, on the other hand, we do attribute the increased intensity of the detected signal to impedance mismatch: in the wings of the MSB, the conversion length is long, thus there is significant signal in the fundamental mode at the end of the device, and this mode has a notably different profile to that of the terminal ridge waveguide, and as such it undergoes a reflection. The backward-propagating fundamental mode then generates the higher order mode which is now propagating forwards. Its extracted part both interferes with the backward-propagating signal and reflects from the waveguide defining trenches at the output. This effect becomes more obvious in simulations of shorter devices. Note, however, that we do not strongly see this behaviour in zone C in the experiment (see Fig. 5a) because the device is tilted such that the backward-propagating HOM exits perpendicularly to the facet, thus the forward-propagating HOM is angled further away. Finally in zone B, both in the FDTD and in the experiment, we see the complex asymmetric pattern attributed to the overall effects of these reflections.

3. Double filtering structure

3.1. Analysis of performances and first-order limitations

Based on this analysis, we present the results of a design intended for CWDM operation and exploiting a wider W7 waveguide with sharper features and more distributed action, which makes it ideal for monitoring applications. The device is designed using a multi-section CMT, assuming mode continuity between sections which we justify on the basis of modest proportional differences in width. We show in Fig. 7a the design of a four-channel device, each channel separated by a spacer comprising a blank channel with MSB out of the demux spectral region which is thinned on both sides to increase its α_s^c value. We are currently

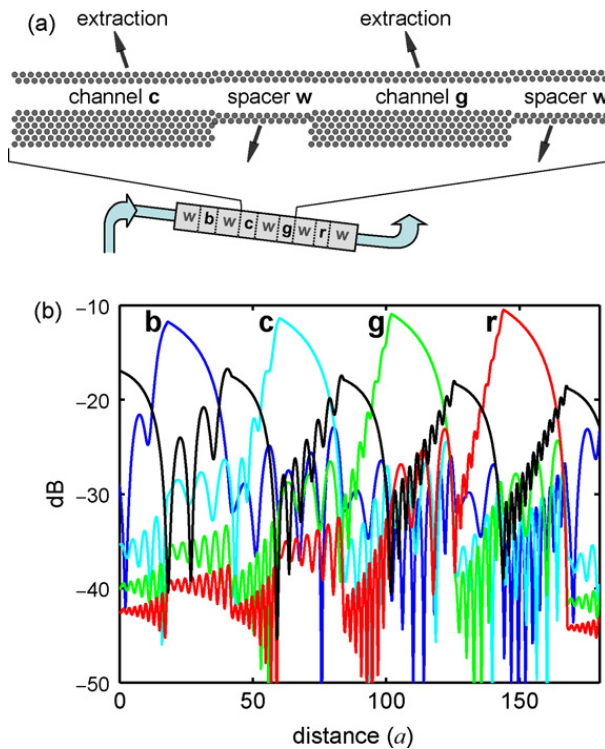


Fig. 7. Four-channel device. (a) Design for one channel. (b) Evolution of the extracted signals (log scale and $a = 400$ nm). The colour codes b , c , g , r in (a) relate to the colours of the response in (b), with the spacer channel in black.

fabricating such a device. The aim of this spacer is to extract the remaining backward-propagating signal in the HOM of each frequency channel, so that this contributes to the output signal rather than the crosstalk in the previous channel. The intensity of the HOM for the centre frequencies of each of the four channels are plotted as function of position in Fig. 7b, as calculated using CMT. This also helps in the physical definition of channels by means of etched trenches, as the peak signal is by definition found at the very entrance to each channel. Such trenches, playing the role of a spatial aperture, may then be optimally centred thereby aiding eventual detection. Further, we remove the significant reflections discussed in the previous section by having spacer sections at the beginning and end of the device, which otherwise will degrade the performance of the first and last channels to be dropped.

With this new design, we see a second contributor to the crosstalk which is less evident without the spacer: for any given frequency channel, the adjacent frequency channels overlap the tails of its MSB and thus their HOM is also generated to some lesser extent. As this adds to the portion of the signal for downstream channels which has been converted but not extracted, the resonance builds up more quickly than from a clean channel. We can use this HOM data to optimize the

choice of integration region [3] with respect to transmission and crosstalk. Briefly, the aperture optimization means that for each frequency channel we include the signal from the end of the upstream spacer, and leave out the end of the spatial channel where the extraction is lowest and the crosstalk contribution highest. An example of this can be seen in the schematic for our next-generation device, discussed in the following section. Models with increased confinement in the regions to be screened by the aperture show enhancement to the resonance and thus greater conversion efficiency for all frequencies. Therefore, care must be taken in the design of the aperture trenches not to suppress the leakage through the thinned sidewall, as small gains in transmission are countered by significant increases in crosstalk.

For given channel spacing and area constraints, then, this regeneration in the MSB tails is the limiting factor on crosstalk performance. The results are comparable with any singly resonant filter, which are generically insufficient for mainstream applications. Here, an optimization of these apertures leads to a typical crosstalk limit on the order of 18 dB. It is thus natural to turn to multiple-cavity structures, as is classical in standard multilayer interference-filter synthesis. We now consider the effects of adding a second Fabry–Perot filter to our device. Such a second filter concept has previously been proposed for PhC devices in Ref. [10], but our approach implements a more naturally integrated improvement.

3.2. Double-filtering structure

A second cavity can be readily added to the exit path of our device, as indicated in Fig. 7, by adding additional rows of PhC on the drop side of each channel at the appropriate distance. These holes should be of type B with respect to the existing structure, *i.e.*, shifted by half a period, to suppress the MSB effect, and should extend across the whole integration region, as discussed above, rather than across the whole channel. The device schematic is outlined in Fig. 8. We possess a particular technological advantage in realizing this device, as the proximity and similarity of the cavities allows an accurate common tuning condition to be obtained in practice. We propose to model this device, in the first instance, by applying a second spatial and frequency-dependent filter to the HOM values calculated in the CMT, and in the case of a lossless filter we find a greater than 14 dB gain in selectivity: The typical crosstalk limit is then found to be better than 32 dB. This is essentially attributable to the Airy function for the

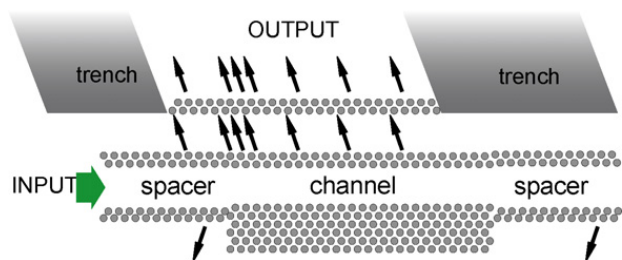


Fig. 8. Double filtering design. The arrows indicate the relative flux strength of the signal.

Fabry–Perot type filter, as the basic W7 operates at 12th order thus we have a very high quality factor. However, the detailed response of this model is very sensitive to the loss and reflectivity of the photonic crystal mirrors, eroding the crosstalk performances by a couple of dB. We are proceeding to explore this issue.

4. Conclusion

We have detailed the use of devices on III–V semiconductors for demultiplexing in a low-selectivity approach, with coarse wavelength spacing. We have evidenced the full behaviour of MSB and extraction on devices based on InP, lending themselves to easy integration in the CWDM context. The first end-fire measurements of this side-extraction device type are presented, and behaviours not seen in previously characterized devices are explained. We have also studied the design of a monitor in some depth. However, the basic crosstalk of single-cavity designs was found to be limited much as in other cavities. To fulfil the need for smaller crosstalk, we propose the design of a double-cavity structure, which is a natural extension of our existing device design and should be realisable with an accurate common tuning condition between the two cavities. This will readily push the performance into the doubly resonant range, with crosstalk well below -25 dB when the signal is collected within the optimized bounds of the proposed demux/monitor sequence.

Acknowledgement

This work is carried out within the framework of the European project FUNFOX under grant IST-004582.

References

- [1] E. Viasnoff-Schwoob, C. Weisbuch, H. Benisty, C. Cuisin, E. Derouin, O. Drisse, G.-H. Duan, L. Legouézigue, O. Legouézigue, F. Pommereau, S. Golka, H. Heidrich, H.J. Hensel, K. Janiak, *Appl. Phys. Lett.* 86 (2005) 101107.
- [2] L. Martinelli, H. Benisty, O. Drisse, E. Derouin, F. Pommereau, O. Legouézigue, G.H. Duan, *IEEE Photonic Technol. Lett.* 19 (2007) 282.
- [3] L. Martinelli, H. Benisty, O. Khayam, G.H. Duan, H. Heidrich, K. Janiak, *IEEE J. Lightwave Technol.* 25 (2007) 2385.
- [4] S. Olivier, M. Rattier, H. Benisty, C.J.M. Smith, R.M. De La Rue, T.F. Krauss, U. Oesterle, R. Houdré, C. Weisbuch, *Phys. Rev. B* 63 (2001) 113311.
- [5] C.G.P. Herben, X.J.M. Leitens, F.H. Groen, M.K. Smit, Low-loss and compact phased array demultiplexer using a double-etch process, in: *ECIO '99, Torino (Italy)*, April 13–16, (1999), pp. 211–214.
- [6] Y. Barbarin, X.J.M. Leijtens, E.A.J.M. Bente, C.M. Louzao, J.R. Kooiman, M.K. Smit, *IEEE Photonic Technol. Lett.* 16 (2004) 2478.
- [7] J. Smajic, C. Hafner, D. Erni, *Opt. Express* 11 (2003) 566.
- [8] T. Niemi, L.H. Frandsen, K.K. Hede, A. Harpoth, P.I. Borel, M. Kristensen, *IEEE Photonic Technol. Lett.* 18 (2006) 226.
- [9] B. Momeni, J. Huang, M. Soltani, M. Askari, S. Mohammadi, M. Rakhshanderoo, A. Adibi, *Opt. Express* 14 (2006) 2413.
- [10] A.S. Jugessur, A. Bakhtazad, A.G. Kirk, L. Wu, T.F. Krauss, R.M. De La Rue, *Opt. Express* 14 (2006) 1632.
- [11] S. Olivier, H. Benisty, C. Weisbuch, C.J. Smith, T.F. Krauss, R. Houdré, *Opt. Express* 11 (2003) 1490.
- [12] H. Kogelnik, C.V. Shank, *J. Appl. Phys.* 43 (1972) 2328.
- [13] H. Benisty, L. Martinelli, E. Viasnoff-Schwoob, M.A. Pinault, C. Weisbuch, G.-H. Duan, H. Heidrich, K. Janiak, I. Robert-Philip, Role of one-dimensional singularities in the operation of some photonic crystal based devices, *Proc. SPIE* 6128 (2006) 126–140.
- [14] M.V. Kotlyar, L. O'Faolain, R. Wilson, T.F. Krauss, *J. Vac. Sci. Technol. B* 22 (2004) 1788.
- [15] <http://www.photond.com/>.
- [16] H. Gersen, T.J. Karle, J.P. Engelen, W. Bogaerts, J.P. Korterik, N.F. van Hulst, T.F. Krauss, L. Kuipers, *Phys. Rev. Lett.* 94 (2005) 073903.